

Mechanistic insight into bifunctional thermocatalytic CO₂ hydrogenation by Oxide-Supported Palladium

Hyuk Choi ^{a,1}, Yejung Choi ^{a,1}, Jongseok Kim ^{a,1}, Ju Hyeok Lee ^a, Eunji Kang ^a, Jieun Yun ^a, Hongjin Park ^a, Minkyung Kim ^a, Habib Ullah ^a, Kihyun Shin ^{b,*}, Hyun You Kim ^{a,*}

^a Department of Materials Science and Engineering, Chungnam National University, Daejeon 34134, Republic of Korea

^b Department of Materials Science and Engineering, Hanbat National University, Daejeon 34158, Republic of Korea

ARTICLE INFO

Keywords:
Heterogeneous catalyst
Palladium
CO₂ hydrogenation
Density Functional Theory
Interface

ABSTRACT

Hydrogenating CO₂ into clean fuels and hydrocarbons such as methane, formic acid, and C₂⁺ products is a viable strategy for mitigating anthropogenic carbon dioxide. Based on density functional theory calculations, we elucidate the mechanism of CO₂ hydrogenation by Pd nanoparticles supported on MgO or CaO. To provide fundamental insight into the rational design of active and selective CO₂ hydrogenation catalysts, we combined Pd, a hydrogen activator, and MgO or CaO, a CO₂ binder. We found that Pd preferentially binds and dissociates H₂, and the Pd-oxide interface activates CO₂, completing a bifunctional CO₂ hydrogenation reaction. The Pd-CaO interface strongly binds CO₂ compared to the Pd-MgO interface. Therefore, the weakened C-O bond enables hydrogenation of the oxygen of CO₂, activating the carboxyl pathway of CO₂ hydrogenation and producing CO and methanol. In contrast, the formate pathway through direct hydrogenation of the carbon of CO₂ operates in the Pd-MgO catalyst due to the relatively weak interaction with CO₂. Producing formic acid and methanol is thermodynamically more accessible in Pd/MgO. Our results show that the catalyst-CO₂ interaction steers the overall reaction pathway of thermocatalytic CO₂ hydrogenation by metal/oxide class heterogeneous catalysts.

1. Introduction

Carbon dioxide (CO₂) is a significant greenhouse gas causing climate change. [1–5] One breakthrough in reducing anthropogenic CO₂ emissions is converting it into valuable products through hydrogenation, such as methanol, formic acid, and methane. [6] Electrochemical conversion is mainstream in CO₂ hydrogenation because the activity and selectivity can be controlled by exerting external potential. However, the low absolute conversion efficiency of electrochemical CO₂ conversion retards its applications in industry. [7] On the other hand, several benefits of thermocatalytic CO₂ conversion, such as high conversion rate and versatility of the reaction products, provide the opportunity for large-scale applications in industry. [8] The reverse water–gas shift reaction (CO₂ + H₂ → CO + H₂O) is the most representative thermocatalytic CO₂ conversion, which generates valuable synthetic gas [9–11].

A substantial electron donor is required to bind and activate gas phase CO₂, thus initiating CO₂ hydrogenation. [12–16] A carbonate-like bent CO₂ with excess electrons is a signature feature of CO₂ activation.

Metal catalysts such as Rh, Ru, and Cu-based catalysts electronically interact with CO₂ and thus are excellent CO₂ activators. [17–21] In addition, the reducible oxides, such as In₂O₃ and CeO₂, strongly bind and activate CO₂ on the oxide surface or at the interfacial site between supported metal NPs. [22–24] Because various types of CO₂ activators with different local atomic ensembles can be utilized to design CO₂ hydrogenation catalysts, subsequent hydrogenation of an activated CO₂ may take several different pathways, [25] which interrupts clarifying the reaction mechanism.

On the other hand, non-reducible oxides, such as MgO, CaO, ZnO, and ZrO₂, have an intense Lewis basicity site, where they interact more strongly with CO₂ than H₂. [26–28] MgO or CaO with relatively high PZC (point of zero charge) values and enhanced surface basicity may further facilitate CO₂ adsorption and activation. [29,30] Such structural basicity in oxide support is generally utilized for effective adsorption of reactants. [31–33] For example, Mg-doped oxide supports exhibit superior CO₂ conversion performances with high product selectivity. [34] Furthermore, nano-sizing MgO and CaO affects the adsorption strength

* Corresponding authors at: Department of Materials Science and Engineering, Hanbat National University, Daejeon 34158, Republic of Korea (K. Shin).

E-mail addresses: kihyun@hanbat.ac.kr (K. Shin), kimhy@cnu.ac.kr (H.Y. Kim).

¹ These authors contributed equally to this work.

of CO₂, thus modulating the catalytic activity [35–38].

Chemical binding of gas phase H₂ and dissociation is thermodynamically feasible and facile on precious metal surfaces. [39–41] If precious metal nanoparticles (NPs) are supported on reducible oxides forming metal-oxide interfaces, the dissociated hydrogen diffuses toward the oxide surfaces, saturating the surface with hydroxyls. [42–44] The Pt- or Pd-based catalysts provide the H₂ activation sites, and the metal-oxide interfaces act as a gateway of H-spillover toward the reducible oxide supports. [42,43,45–47] The Pd-based catalysts exhibit high selectivity for carbon monoxide (CO) and methanol (CH₃OH), depending on the type of oxide support [31].

From a rational catalyst design perspective, identifying the location and the chemical state of the reaction site is essential. [48–53] However, it becomes challenging if two or more comprising elements of the

catalyst system have different catalytic roles. A typical case is the thermocatalytic CO₂ hydrogenation by bifunctional catalysts with both CO₂ and H₂ activators. Moreover, the catalytic role of the inter-materials interface varies depending on the dimension and the size of each material and the structural evolution of the atomic ensembles at the interfaces under the reaction conditions. [54–57] In this aspect, illustrating the overall mechanism of thermocatalytic CO₂ hydrogenation based on a well-modeled heterogeneous catalyst aids in identifying the active site and clarifying activity-determining factors.

Here, we use a model catalyst composed of Pd NPs and supporting oxides to study the mechanism of CO₂ hydrogenation by density functional theory (DFT) calculations. A Pd NP, which binds H₂ and dissociates into H atoms, was supported on MgO or CaO, which binds and activates CO₂. Using carbonate-forming MgO and CaO as a supporting

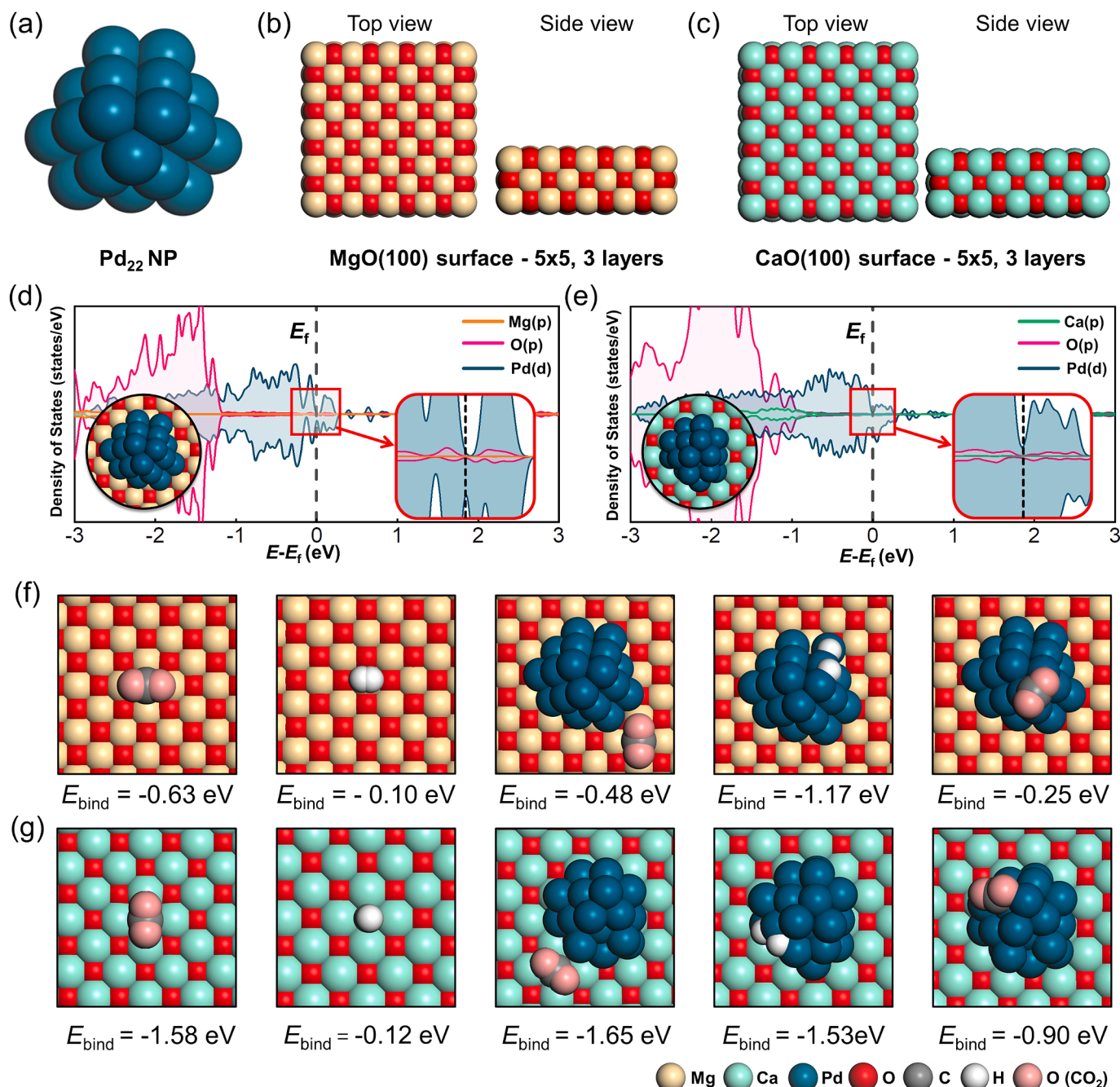


Fig. 1. DFT-optimized structural models of (a) Pd₂₂ NP, (b) MgO (100), and (c) CaO (100), respectively. The projected density of states plots of (d) Pd/MgO and (e) Pd/CaO. Most preferred adsorption sites and energy (E_{bind}) of H₂ and CO₂ on (f) Pd/MgO and (g) Pd/CaO.

material, we focus on the mechanism of CO₂ hydrogenation at the Pd-oxide interfaces. Our DFT-estimated reaction diagrams identified the Pd-oxide interfaces as reactive species. We found that the CO₂ binding strength at the Pd-oxide interface steers the reaction pathway of CO₂ hydrogenation.

2. Density functional theory calculations

We used a Pd₂₂ NP supported on a 5 × 5 × 3 periodic supercell slab of MgO(100) or CaO(100). A 15 Å vacuum layer was applied on both systems to avoid the interaction between periodic cells. The bottom layer of MgO and CaO was fixed during geometry optimization. A cuboctahedral-like 3-layered Pd NP was supported on MgO and CaO and appropriately optimized (Fig. 1a-c).

We performed spin-polarized DFT calculations using a plane-wave basis with the Vienna Ab-initio Simulation Package [58] and the PBE (Perdew-Burke-Ernzerhof) [59] exchange–correlation functional. The DFT-D3 van der Waals correction method [60] with the Becke-Johnson damping model was applied to improve the reliability of the results. The interaction between the ionic core and the valence electrons was described by the projector-augmented wave method [61,62]. Valence electron wave functions were expanded on a plane-wave basis up to an energy cutoff of 400 eV. The Brillouin zone was sampled at the Γ -point for all calculations. The convergence criteria for the electronic structure and the atomic geometry were 10⁻⁴ eV and 0.05 eV/Å to optimize all geometries. To secure the accuracy of the electronic structure, we set the convergence criteria to 10⁻⁶ eV for all electronic structure and frequency calculations. We used a Gaussian smearing function with a finite temperature width of 0.05 eV to improve the convergence of states near the Fermi level. The location and the energy of transition states (TSs) were estimated using the climbing-image nudged elastic band method. [63,64] A subsequent normal mode of frequency analysis was performed to confirm the morphological reliability of all TS. The projected Crystal Orbital Hamilton Population (*p*COHP) analysis was performed with the LOBSTER code [65,66].

The relative coverage of hydrogen on Pd₂₂ NP was estimated by calculating the ΔG of adsorption. The ΔG of H₂ and CO₂ adsorption was calculated as follows:

$$\begin{aligned} \Delta G = & E(\text{Catalyst} + \text{H}_2, \text{CO}_2) - E(\text{Catalyst}) - [E(\text{H}_2, \text{CO}_2) \\ & + \Delta\mu(\text{H}_2, \text{CO}_2)] \end{aligned} \quad (1)$$

where $E(\text{Catalyst} + \text{H}_2)$ and $E(\text{Catalyst})$ present the DFT-estimated total energy of a catalyst with adsorbed CO₂ or H₂ or a bare catalyst surface, respectively. The chemical potential of H₂ and CO₂, $\Delta\mu(\text{H}_2 \text{ and } \text{CO}_2)$, the chemical potential difference, is given by

$$\begin{aligned} \mu_{\text{gas}}(T, p) &= \Delta H(0K, p^0 \rightarrow T, p^0) - T\Delta S(0K, p^0 \rightarrow T, p^0) + kT\ln(p/p^0) \\ \Delta\mu_{\text{gas}} &= \mu_{\text{gas}}(T, p) - E(\text{gas}) \end{aligned} \quad (2)$$

where p^0 is set to 1.013 bar and $\mu_{\text{gas}}(0K, p^0) = E(\text{gas})$. Tabulated temperature-dependent enthalpy and entropy values of H₂ were adopted from the NIST chemistry webbook [67].

In other words, the entropy of adsorbed CO₂ is considered the adsorption entropy, as suggested by Campbell's experimental findings [68]. The following linear relationship between the entropy of a gas-phase molecule and an adsorbed molecule was applied:

$$\Delta S_{\text{bind}} = S_{\text{adsorbed}}^0 - S_{\text{gas}}^0 = (0.7S_{\text{gas}}^0 - 3.3R) - S_{\text{gas}}^0 \quad (3)$$

where S_{gas}^0 represents the standard entropy of gas phase molecules. In this case, the effect of the $-T\Delta S$ on the Gibbs free energy of adsorption is limited to 30 % of the conventional estimation. Based on the contributions of the adsorption entropy of CO₂, we confirm the limitation of adsorption on catalysts.

3. Results and Discussion

3.1. Adsorption of CO₂ and H₂ on Pd/MgO and Pd/CaO

Fig. 1 presents the morphology of the DFT-constructed Pd/MgO and Pd/CaO and each component. The projected density of states (*p*DOS) diagrams show that Pd is electronically well-coupled with supporting oxides (Fig. 1d and 1e). To model the initial equilibrium surface states of the catalysts under the CO₂ hydrogenation conditions, we calculated the CO₂ and H₂ binding energy, E_{bind} , on MgO, CaO, Pd/MgO, and Pd/CaO (Fig. 1f and 1 g). Like the consensus about the CO₂ capturing ability of nano-sized alkaline metal oxides, [35,36,69] MgO and CaO preferentially bind CO₂ to H₂. The MgO surface relatively weakly binds CO₂ with E_{bind} of -0.63 eV, whereas the CaO surface binds CO₂ strongly ($E_{\text{bind}} = -1.58$ eV). This binding trend in MgO and CaO was consistent even after supporting a Pd NP within ± 0.2 eV of the window, meaning that the surfaces and the Pd-oxide interfaces will be covered with CO₂ under the reaction conditions, irrespective of the CO₂ partial pressure (Fig. 1f and 1 g).

On the other hand, the Pd surface dissociatively binds H₂. The E_{bind} of H₂ is more than ten times greater on Pd NPs than on oxide surfaces, indicating that Pd NPs activate H₂ for CO₂ hydrogenation (Fig. 1f and 1 g, the conventional reactant ratio in feeding gas; H₂:CO₂ = 4:1) [11,22,23,70–74]. We noted that our Pd/MgO and Pd/CaO catalysts spatially separately bind CO₂ and H₂, clearly distinguishing the activation sites of CO₂ and H₂. Such a bifunctional role of the components assures a poison-free reaction mechanism with high versatility [75].

Based on the DFT-calculated E_{bind} of CO₂ and H₂, we determined the hydrogen surface coverage on Pd by converting E_{bind} to ΔG of H adsorption considering the temperature and pressure windows. The sequential E_{bind} of H on Pd (Figure S1) calculated according to the increasing hydrogen coverage from 2H atoms (1/9 ML) to 18H atoms (1 ML), confirms that Pd affords 1 ML of hydrogen at 298 K. Since CO₂ cannot access the Pd NP surface during competitive adsorption of H₂ and CO₂, we estimated the surface H coverage of Pd NP with the ΔG of H adsorption on Pd as a function of the $\Delta\mu_{\text{H}}$ (Fig. 2a-b). The orange boxes below Fig. 2a and 2b represent the available range of $\Delta\mu(\text{H}_2)$ at 700 K, 600 K, and 400 K ($1 \leq p(\text{H}_2) \leq 30$ atm). The temperature and H₂ partial pressure adjusted ΔG diagrams of H adsorption (Fig. 2a and 2b) and the projected coverage maps (Fig. 2c and 2d) indicate that Pd NPs bind up to 1 ML of hydrogen under the experimental CO₂ hydrogenation conditions (literature reported conditions, yellow dots, Fig. 2c). [76–87] This information is essential for DFT-based mechanism studies because the last-binding hydrogen weakly interacts with Pd, which becomes the most reactive hydrogen. Using the first binding H for CO₂hydrogenation is highly likely to deduce a biased result with endothermicity and high barriers due to the strong Pd-H interaction. We used the model with 1 ML of hydrogen coverage on Pd for subsequent CO₂ hydrogenation studies.

Hydrogen activation on metal NPs and subsequent spillover to the supporting oxide surfaces driven by energetic preference of hydroxyl formation is well-reported on reducible oxides. [88] The hydroxyls on the reducible oxide surfaces may interact with each other or with other surface adsorbates, generating various reaction intermediates. The reaction pathways become complicated accordingly, reducing the selectivity. [89] On the other hand, the inherent tendency toward carbonate formation of MgO and CaO prevents hydrogen diffusion to the oxide surfaces. The calculated E_{bind} values of CO₂ at the Pd/MgO and Pd/CaO interfaces show that the hydrogen-saturated Pd/MgO and Pd/CaO bind single or multiple CO₂ at the Pd-oxide interfaces (Figures S2, S3, and S4). The stronger average CO₂ E_{bind} at the Pt-oxide interfaces (Figures S4a and S4b) than the E_{bind} of H₂ (Fig. 1f and 1 g) spatially localizes hydrogen to the surface of Pd NPs. The H* on Pd NPs diffuses directly to the adsorbed CO₂ at the Pd-oxide interfaces and interacts with CO₂.

Interestingly, the E_{bind} of CO₂ significantly differs in Pd/CaO and Pd/

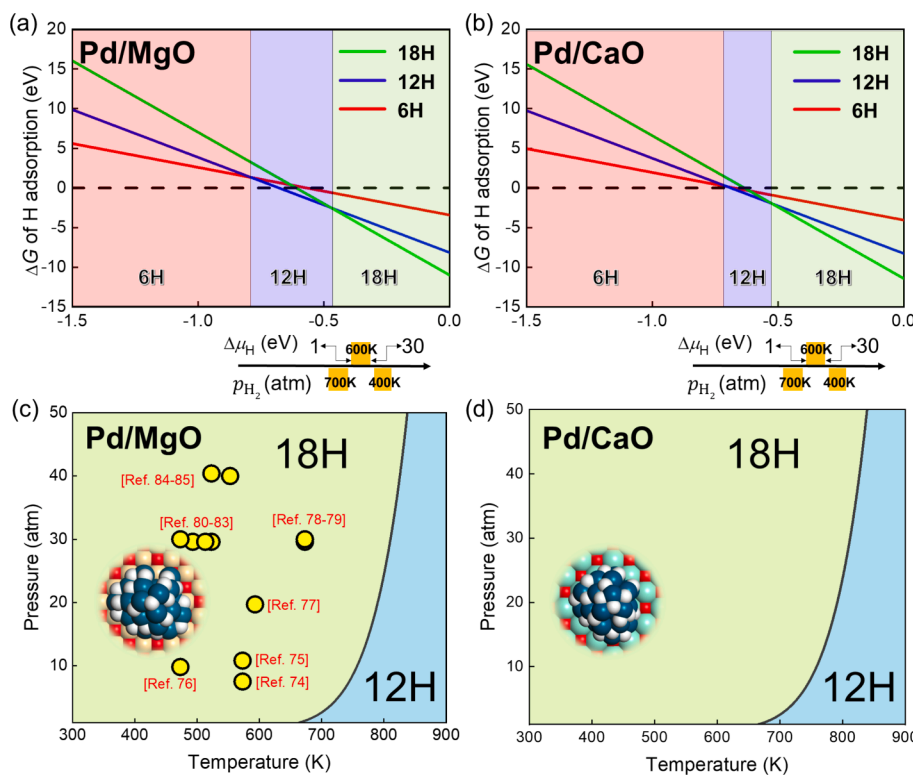


Fig. 2. Equilibrium hydrogen coverage of Pd NPs under the hydrogenation reaction conditions. (a and b) The H adsorption free energy diagram regarding hydrogen coverage on Pd NPs as a function of the chemical potential of hydrogen. The nH indicates the number of H atoms adsorbed on a Pd NP. The indicators below (a) and (b) present the accessible chemical potential range under the reaction conditions. (c and d) Equilibrium surface states of a Pd NP on MgO or CaO under the hydrogenation conditions. The yellow circles indicate the literature-reported experimental hydrogenation reaction conditions (refer to the main text for references).

MgO ($E_{\text{bind}} = -1.16$ eV/CO₂ in Pd/CaO and -0.32 eV/CO₂ in Pd/MgO, respectively, **Figure S4**). Such a difference in CO₂ binding activates different hydrogenation pathways in Pd/CaO and Pd/MgO.

3.2. Initiation of CO₂ hydrogenation at Pd-oxide interfaces

The CO₂ hydrogenation commonly proceeds through the formation of CO⁻, HCOO⁻ or HOCO⁻, depending on the extent of the interaction between CO₂ and catalysts [90–92]. We utilized the H-saturated Pd/MgO and Pd/CaO catalysts to estimate the reaction pathway and the corresponding energetics of CO₂ hydrogenation. We hypothesized that the surface of Pd NPs is constantly saturated with H under the reactions. Because the Pd-MgO and Pd-CaO interfaces bind CO₂ molecules, we constructed the reaction pathway by hydrogenating CO₂ with adjacent H on the Pd surface.

Fig. 3 shows the initial steps of CO₂ hydrogenation by Pd/MgO (**Fig. 3a**) and Pd/CaO (**Fig. 3b**). Note that these catalysts bind CO₂ with different strengths. At the Pd-MgO interface, the CO₂ hydrogenation proceeds by generating formate (**Fig. 3a**). The carbon of CO₂ draws the first hydrogen, forming a formate intermediate (*HCOO) with ΔE of -0.74 eV and E_a of 0.89 eV (S2 and TS1, **Fig. 3a**). The formate formation at the Pd-MgO interface was energetically preferred to the carboxyl (*COOH) formation ($\Delta E = -0.64$ eV) because the relatively weak interaction between CO₂ and Pd/MgO ($E_{\text{bind}} = -0.47$ eV) enables the MgO-C bond breaking. The 31 % higher E_a of the carboxyl formation ($E_a = 1.17$ eV, **Figure S5**) at the Pd-MgO interface confirms that the Pd/MgO catalyst propels the formate formation (**Fig. 3a and S5**). The further hydrogenation of formate to formic acid (*HCOOH), requires a single step with $\Delta E = 0.01$ eV and $E_a = 1.13$ eV (**Fig. 3a and S6**).

On the other hand, the Pd/CaO catalyst strongly binds CO₂ ($E_{\text{bind}} = -1.73$ eV); thus, the hydrogenation starts from the protruded oxygen side (S2, **Fig. 3b**, $\Delta E = 0.36$ eV and $E_a = 0.86$ eV), generating a carboxyl

intermediate, *COOH, at the Pd-CaO interface. The formation of formate is prohibited with ΔE of 0.55 eV and E_a of 3.22 eV (**Figure S7**) because of the strong CaO-C bonding. A water molecule was produced and released upon further hydrogenation of carboxyl (S2 to S5, **Fig. 3b**). Although the CO₂ hydrogenation at the Pd-CaO interface requires a lower E_a than the E_a of Pd/MgO, the first hydrogenation of CO₂ (carboxyl formation, S1 to S2, **Fig. 3b**) and the dissociation of carboxyl into *CO and *OH (S2 to S3, **Fig. 3b**) are energetically uphill. Besides, although the dissociation of carboxyl into *CO and *OH is endothermic ($\Delta E = 0.53$ with E_a of 0.84 eV), the pathway toward formic acid formation from carboxyl (*COOH + *H → *HCOOH) is kinetically forbidden ($\Delta E = -0.47$ eV and $E_a = 2.59$ eV, **Figure S8**). The intense interaction between CO and late transition metals such as Pd, Pt, and Au through π back-donation, [93–96] may decrease the E_a of carboxyl dissociation.

Our DFT calculation results show that the E_{bind} of CO₂ at the Pd-oxide interfaces steers the reaction pathway of CO₂ hydrogenation. The hydrogenation of the relatively weakly bound CO₂ at the Pd-MgO interface is overall exothermic, whereas hydrogenating the strongly bound CO₂ at the Pd-CaO is energetically uphill. Although the dehydrogenation of formate to formic acid (S2 to S3, **Fig. 3a**) requires the highest E_a of 1.13 eV, the forward reaction is always thermodynamically driven in Pd/MgO. However, despite the lower E_a value of each step, the forward reaction (hydrogenation) is thermodynamically uphill, and instead, the backward reactions may easily occur in Pd/CaO. Even once each hydrogenation step proceeds, for example, from S1 to S2, backward dehydrogenation of S2 to S1 is facile so that the lifespan of S2 is short (**Fig. 3b**). Increasing the hydrogen partial pressure in the reaction feedstock may accelerate the forward CO₂ hydrogenation in Pd/CaO according to Le Chatelier's principle.

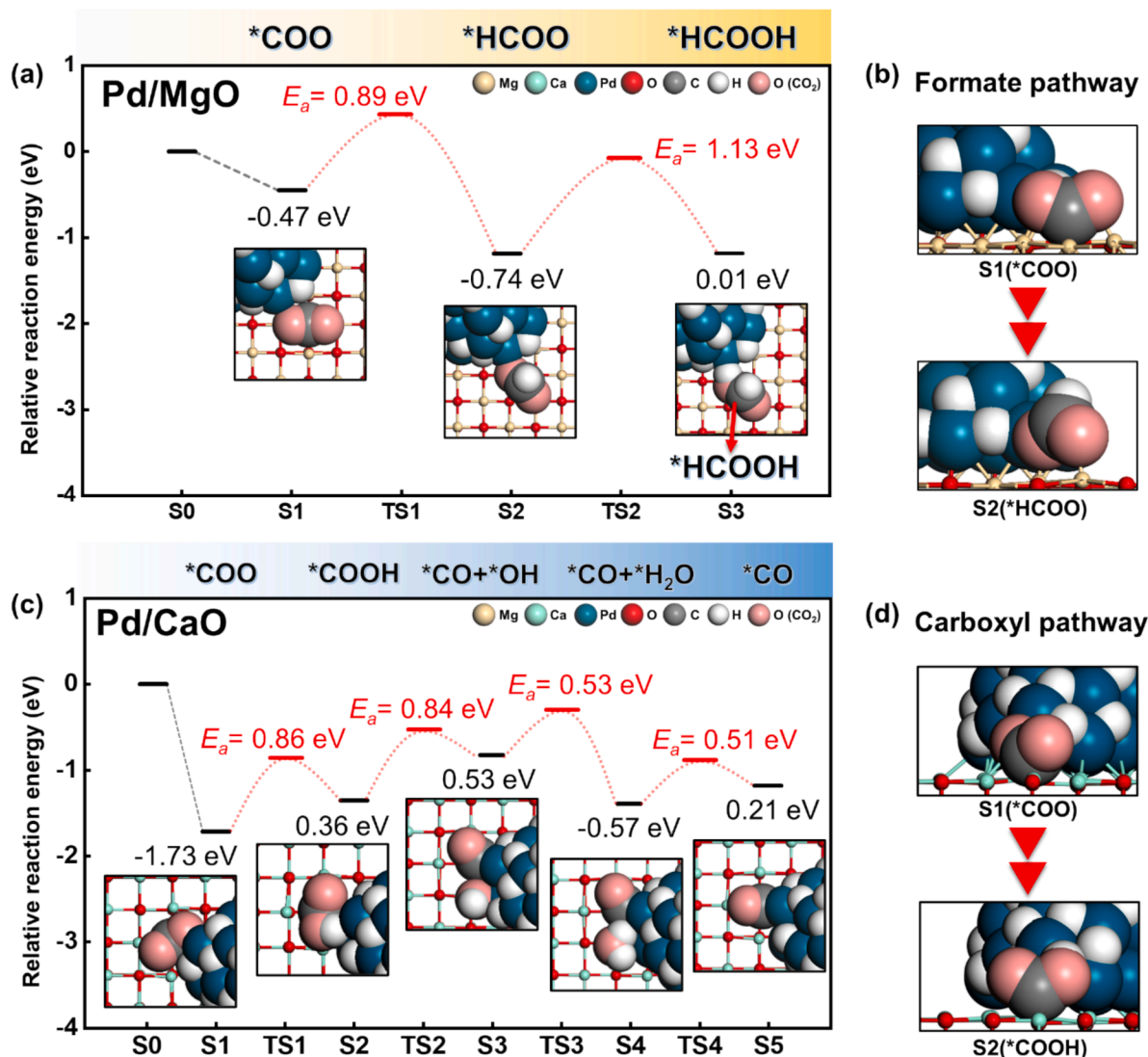


Fig. 3. DFT-estimated reaction pathway and corresponding energetics of CO_2 hydrogenation reaction catalyzed by (a) Pd/MgO and (c) Pd/CaO. (b) and (d) shows the side view of the key intermediate. The S_n and TS_n indicate the n^{th} reaction and transition stages. The black-colored energy values present the reaction energy of the n^{th} step calculated by $\Delta E_n = E_n - E_{n-1}$. The E_a indicates an activation barrier. Single imaginary frequencies for all TS images are presented in Tables S1 and S2.

3.3. Complete CO_2 hydrogenation by Pd/MgO and Pd/CaO

The relevant experimental studies reported methanol as the final product of CO_2 hydrogenation catalyzed by MgO- and CaO-based catalysts. [37,38,91,97] To comparatively study the reaction mechanism of Pd/MgO and Pd/CaO, we constructed a complete CO_2 hydrogenation pathway on Pd/MgO (Fig. 4) and Pd/CaO (Fig. 5). On Pd/MgO, formic acid can be released from the catalyst, closing the hydrogenation loop (S3 to S4', Fig. 4). In this case, formic acid becomes the sole product without side products such as CO or H_2O . However, once further hydrogenation of formic acid occurs from S3 to S4 (Fig. 4), a water molecule is released (S5), and the carbon atom of the remaining ${}^*\text{HCO}$ draws two more hydrogen, transforming to ${}^*\text{CH}_3\text{O}$ (S8). After additional hydrogenation of the oxygen atom of ${}^*\text{CH}_3\text{O}$, methanol is produced (S9'). The high E_a of 2.08 eV (TS5) makes further hydrogenation of methanol to methane scarce. The highest E_a (1.10 eV) comes from the initial hydrogenation of formic acid (TS3). Overall, the energetics of the reaction pathway of Pd/MgO predicts that Pd/MgO produces a mixture of formic acid and methanol (except for steam). A marginal amount of methane can be mixed in the product.

Because the early hydrogenation of ${}^*\text{HCOO}$ to formic acid exhibits the highest E_a through overall CO_2 hydrogenation by Pd/MgO ($E_a =$

1.13 eV, TS2, Fig. 3), this step does not account for the selectivity of the product. The energy profile presented in Fig. 4 instead shows that the balance between the E_{prod} from S3 to S4' (formic acid production and release) and the E_a of subsequent hydrogenation of formic acid (TS3) likely affects the ratio between formic acid and methanol in the product. The E_{prod} of 1.16 eV may be lowered at high temperatures due to the entropic contribution to the Gibbs free energy of desorption. In addition, ΔE from S3 to S4 (0.39 eV, Fig. 4) and the corresponding E_a of 1.10 eV could decrease as the hydrogen partial pressure increases. Presumably, these absolute energy values may also vary according to the size of Pd NPs, the surface facet of MgO, or the presence of dopants within the MgO matrix. Even though it is preliminary to suggest the decisive quantitative analysis result of the product concentration, our findings present the critical reaction steps that influence the product selectivity of thermo-catalytic CO_2 hydrogenation by Pd/MgO.

As a result of the initial hydrogenation of CO_2 along the carboxyl pathway, a CO molecule is left at the Pd-CaO interface of Pd/CaO (S5, Fig. 5). Direct CO desorption from the Pd-CaO interface is energetically less driven than continuous hydrogenation of CO (S6' and TS5, Fig. 5). Similar to the case of Pd/MgO, the carbon of CO draws hydrogen from Pd, forming a ${}^*\text{CH}_2\text{O}$ intermediate (S7, Fig. 5). Through subsequent hydrogenation, the ${}^*\text{CH}_2\text{O}$ intermediate was transformed into methanol.

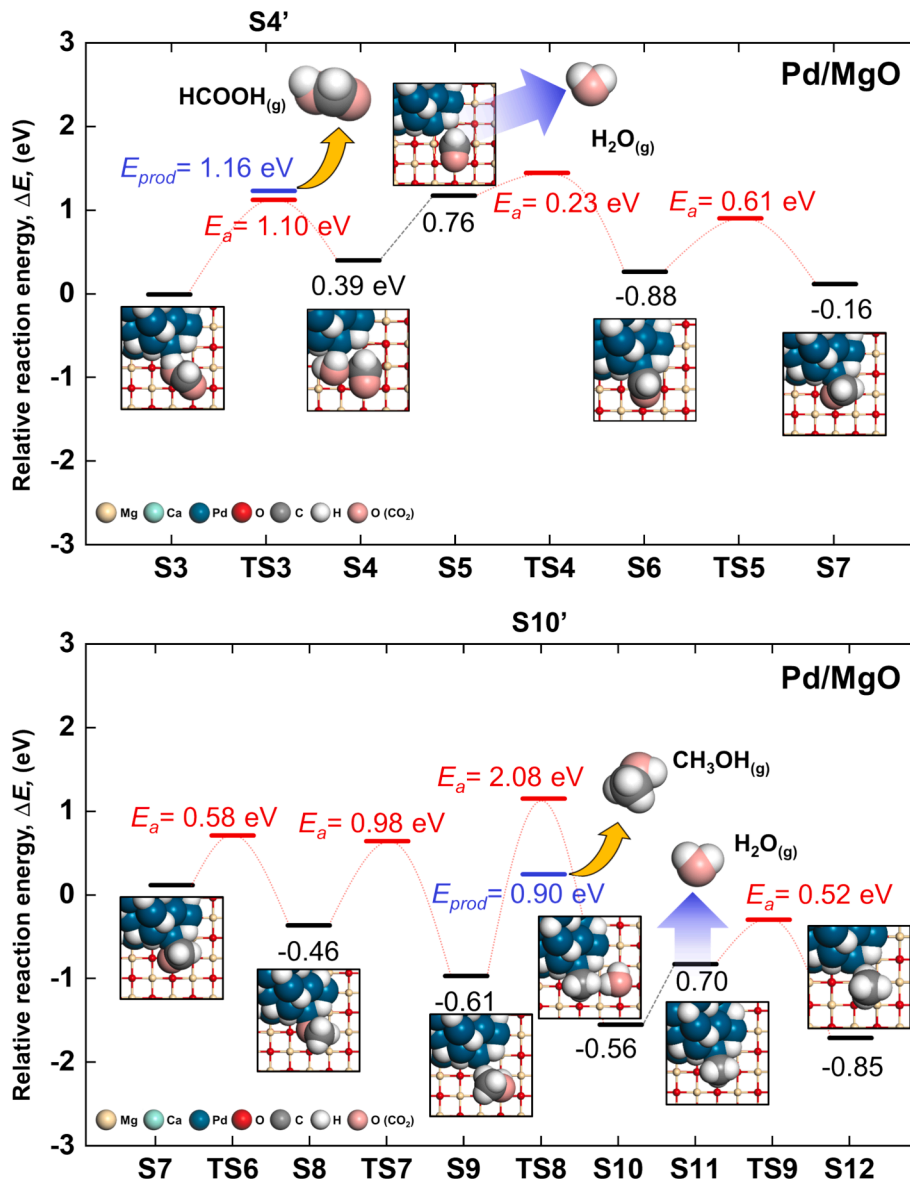


Fig. 4. DFT-estimated sequential reaction pathway and corresponding energetics of CO_2 hydrogenation by Pd/MgO. The Sn and TSn indicate the nth reaction and transition stages. The black-colored energy values present the reaction energy of the nth step calculated by $\Delta E_n = E_n - E_{n-1}$. The E_a indicates an activation barrier. The S3 is identical to the final state presented in Fig. 3a. The E_{prod} (blue state) indicates the energy of the product desorption from the catalyst. We used the Sn', for example, S10', to separately denote the state after product desorption. Single imaginary frequencies for all TS images are presented in Tables S3 and S4.

The highest E_a of 1.65 eV (TS8) originated from the final hydrogenation step, converting $^*\text{CH}_2\text{OH}$ into methanol. The energy of methanol production, $E_{\text{prod}} = 0.93$ eV (S9'), from Pd/CaO is almost identical to that from Pd/MgO (0.90 eV). The high E_a of 2.68 eV (TS9) prevents the formation of methane (S9 to S13).

Like the case of Pd/MgO, the E_{prod} of CO ($E_{\text{prod}} = 1.56$ eV, S6', Fig. 5) can be reduced due to the entropic contribution to the Gibbs energy. However, the relatively low E_a of 0.66 eV toward hydrogenation of $^*\text{CO}$ to $^*\text{HCO}$ (TS5, Fig. 5) may kinetically facilitate hydrogenation of $^*\text{CO}$. Nevertheless, the highest E_a of 1.65 eV over all DFT-estimated reaction steps by Pd/MgO and Pd/CaO (TS8, Fig. 5) is found at the final dehydrogenation of $^*\text{CH}_2\text{OH}$ to methanol, meaning that methanol formation by Pd/CaO is kinetically sluggish. If sufficient thermal energy to overcome the TS8 is supplied, the final product of CO_2 hydrogenation by Pd/CaO is highly likely a mixture of CO and methanol. The relative concentration of methanol may increase under high hydrogen partial pressure conditions.

3.4. Discussion

The difference in the CO_2 hydrogenation reaction pathways of Pd/MgO and Pd/CaO stems from their interaction strength with CO_2 . We found that CO_2 interacts more intensely with CaO than MgO, regardless of whether Pd NP is supported (Fig. 1, Fig. 6a). The energy of CO_2 chemisorption on oxide is closely related to the bonding chemistry and electronic interactions with oxide and CO_2 . We characterized the electronic interaction upon CO_2 adsorption on MgO and CaO by charge density difference plots and Bader charge analysis (Fig. 6b). A typical bent CO_2 on MgO and CaO presents electron transfer from the support to CO_2 . [17] The Bader charge analysis result indicates that MgO and CaO donate a similar amount of electrons to CO_2 ($\Delta\rho = -0.38$ e and -0.41 e, respectively). Furthermore, the orbitals associated with electronic interaction between CO_2 and support are identical on MgO and CaO. These results indicate that the extent of the electronic interaction between CO_2 and oxides is not a primary reason for the difference in the E_{bind} .

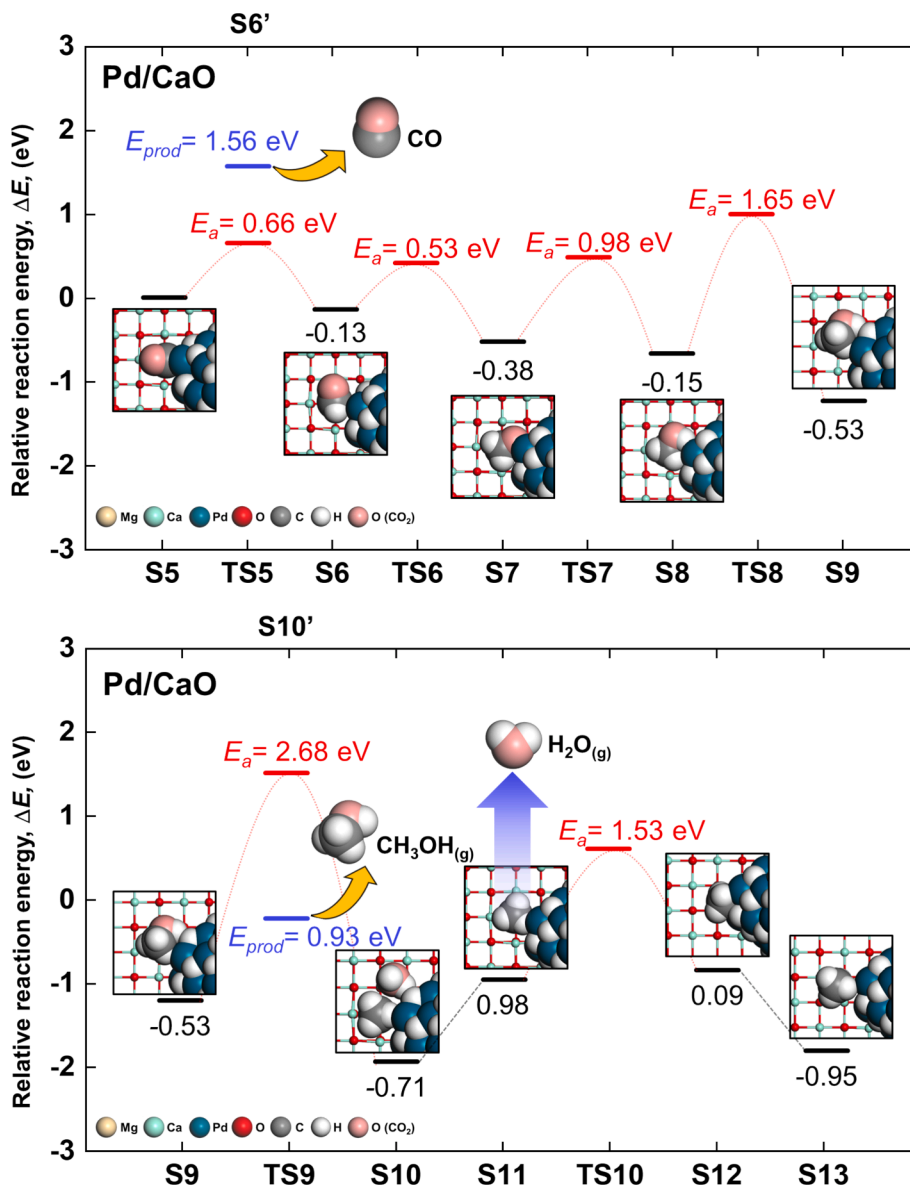


Fig. 5. DFT-estimated sequential reaction pathway and corresponding energetics of CO_2 hydrogenation by Pd/CaO. The Sn and TSn indicate the n^{th} reaction and transition stages. The black-colored energy values present the reaction energy of the n^{th} step calculated by $\Delta E_n = E_n - E_{n-1}$. The E_a indicates an activation barrier. The S3 is identical to the final state presented in Fig. 3a. The E_{prod} (blue state) indicates the energy of the product desorption from the catalyst. We used the Sn', for example, S10', to separately denote the state after product desorption. Single imaginary frequencies for all TS images are presented in Tables S3 and S4.

On the other hand, Fig. 6b shows noticeable differences in the bond lengths and the bond angle of CO_2 on MgO and CaO . The C-O bond length between the carbon of CO_2 and the surface oxygen of CaO (1.41 \AA) was decreased from that of CO_2 on MgO (1.45 \AA), representing the stronger $\text{CO}_2\text{-CaO}$ interaction. The intense interaction between CaO and CO_2 makes the internal C-O bonds within CO_2 increase on CaO (1.27 \AA) compared with MgO (1.26 \AA), enabling the preferred hydrogenation of the oxygen side of CO_2 , initiating the carboxyl pathways.

The pDOS and projected Crystal orbital Hamilton Population (pCOHP) analysis present a straightforward view of the orbital-pair interaction between CO_2 and oxide supports (Fig. 6c and 6d). The pDOS plots show that the carbon p -orbital of CO_2 morphologically overlaps with the oxygen p -orbital of oxides, forming the energy states near the Fermi level. Generally, the positive and negative spectra in the pCOHP plots correspond to the bonding and the antibonding states, respectively. The pCOHP plots of CO_2 on MgO and CaO show an entirely different nature of CO_2 bonding on MgO and CaO . The pCOHP profile of CO_2 on MgO shows the rich antibonding states below the Fermi level

(Fig. 6c). In contrast, the bonding states occupy the same energy window in CO_2 on CaO (Fig. 6d), confirming that CO_2 is relatively strongly interacting with CaO .

We further analyzed the morphology of the molecular orbitals (MOs) of adsorbed CO_2 on MgO and CaO to visualize the MOs bringing the difference in the pCOHP spectra (Fig. 7). Upon CO_2 adsorption on MgO and CaO , the lone pair (non-bonding), $3 \sigma_g^*$, and $2 \pi_u^*$ (antibonding) CO_2 orbitals (refer to Figure S9 for MOs of a gas phase CO_2) generate the MOs near the Fermi level. The pDOS plots of the adsorbed CO_2 and the lattice oxygen of supporting oxides interacting with CO_2 show that the morphology of the highest occupied MO (HOMO) differs in the two systems (Figure S8).

The overall frontier orbitals mainly exhibit the π bonding characters resulting from the interactions between the oxygen p -orbitals and CO_2 MOs. On MgO , the low-energy orbitals appear upon interactions between the oxygen p -orbitals and the $2 \sigma_g$, $1\pi_u$, $2 \sigma_u^*$, and lone pair of CO_2 (Fig. 1a). On the other hand, the lone pair orbital of CO_2 generated the

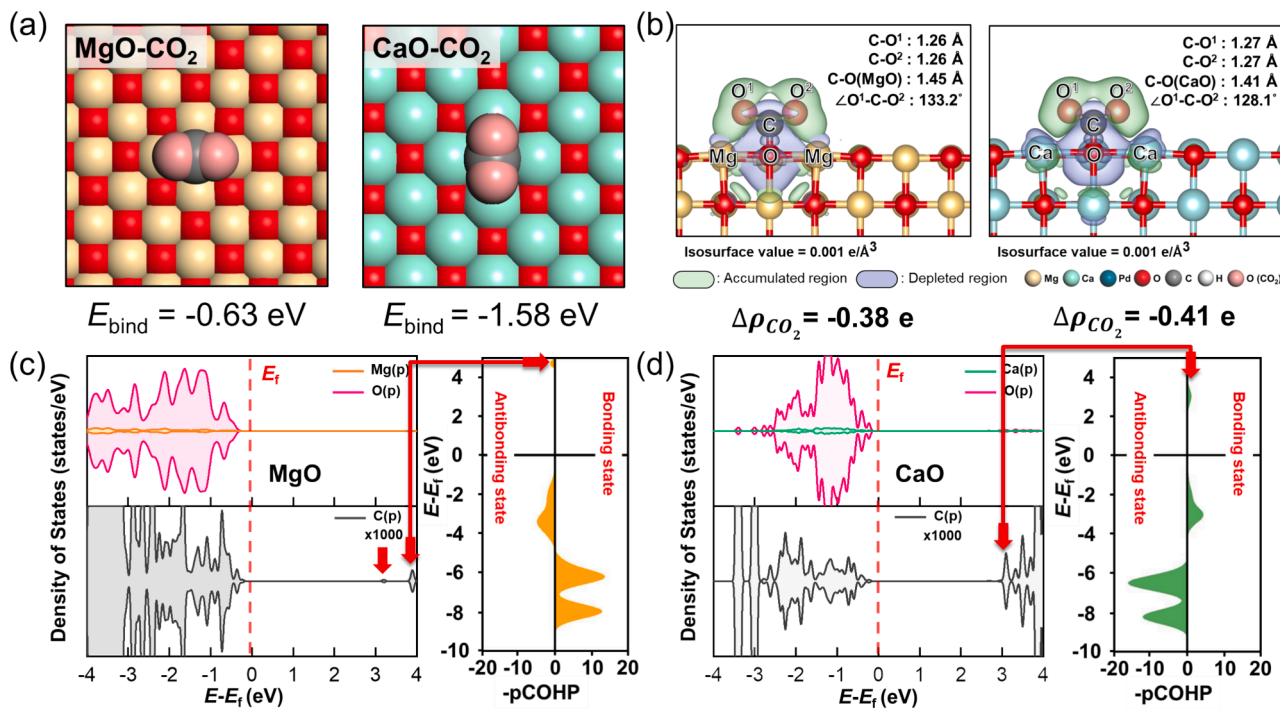


Fig. 6. Electronic analysis of the bonding chemistry of CO₂ on Pd/MgO and Pd/CaO. (a) DFT-calculated binding energies of adsorbed CO₂ on MgO and CaO. (b) Charge difference diagram of adsorbed CO₂ on MgO and CaO. The isosurface presents the orbital that participates in CO₂ adsorption. (c and d) pDOS and pCOHP of adsorbed CO₂ on MgO and CaO. The red arrows indicate the energy and bonding states corresponding to the LUMO state.

antibonding HOMOs with the in-plane oxygen *p*-orbitals of MgO, reproducing the pCOHP analysis result, indicating that the antibonding nature of the HOMO is responsible for the relatively low E_{bind} of CO₂ on MgO (Fig. 1a).

The bonding HOMO of CO₂ on CaO forms upon hybridization between 2 π_u^* of CO₂ and the in-plane oxygen *p*-orbitals of CaO (Fig. 1b). Because the antibonding 2 π_u^* orbital of a gas phase CO₂ draws electrons from CaO, the internal C-O bonds of CO₂ are stretched. (Fig. 7b). The bonding MOs near the Fermi level confirm the strong interaction between CO₂ and CaO.

Several previous experimental studies on CO₂ hydrogenation by Pd/MgO report a high and a low selectivity toward methanol and formic acid, respectively, [28,98] conflicting with our DFT-predicted reaction energetics. This phenomenological discrepancy likely appears due to the high hydrogen partial pressure applied under the experimental CO₂ hydrogenation conditions. Interestingly, the DFT-estimated reaction energetics show that the ΔE from S3 to S4 (Fig. 4) and the corresponding E_a (TS3, Fig. 4) could accordingly decrease as the hydrogen partial pressure increases due to Le Chatelier's principle. Our DFT study results indirectly predict that increasing the hydrogen partial pressure is essential in producing methanol through CO₂ hydrogenation by Pd/MgO.

The relevant experimental study shows that Pd/CaO produces a mixture of CO and methanol upon CO₂ hydrogenation. [99] Our DFT-estimated energetics of CO₂ hydrogenation by Pd/CaO (Figs. 3 and 5) shows the higher production energy of CO compared to the activation energy of further hydrogenation (TS5 and S6', Fig. 5) step, indicating that the production of CO is energetically less preferred. However, we note that the energy of CO production (desorption) can also be reduced at high reaction temperatures. In addition, the inter-molecular repulsion between the CO molecules formed at the Pd-CaO interfaces may assist CO production [100].

Our results suggest that high-PZC oxides such as MgO and CaO with strong surface basicity are adequate for CO₂ hydrogenation reactions, promoting CO₂ adsorption and activation. We found that CaO with a

relatively higher PZC exhibits a higher CO₂ binding energy than MgO, activating the COOH-mediated reaction pathway rather than the HCOO-mediated one. This result suggests that a direct and precise correlation may exist between the PZC value of oxide supports and the selectivity of CO₂ hydrogenation. Although supported metal nanoparticles on oxides concurrently modulate the overall energetics of CO₂ hydrogenation and the thermodynamic preference toward a specific reaction product, we hypothesize that the PZC can be utilized as a designing factor for CO₂ hydrogenation by supported metal nanoparticle class heterogeneous catalysts.

4. Conclusion

Herein, we performed DFT calculations to elucidate the reaction mechanism of CO₂ hydrogenation by Pd/MgO and Pd/CaO. By combining H₂-activating Pd with CO₂-activating MgO or CaO, we design a bifunctional CO₂ hydrogenation catalyst with active species at the Pd-oxide interfaces. Interestingly, our results show that the initial CO₂ binding strength at the Pd-oxide interfaces determines which kind of reaction intermediate is preferentially formed and, thus, what kind of product is produced. The carbonate pathway is activated on Pd/CaO with the relatively higher E_{bind} of CO₂. On the other hand, the lower E_{bind} of Pd/MgO allows direct hydrogenation of the carbon of CO₂, enabling the formate pathway of CO₂ hydrogenation. Through electronic structure analyses, we found that the morphology of the HOMOs of CO₂ on Pd/MgO and Pd/CaO accounts for the binding strength of CO₂ on the catalysts. By comparing with relevant experimental reports, we confirm that our DFT study results provide a fundamental understanding of thermocatalytic CO₂ hydrogenation by Pd-based catalysts that aid the rational design of better-performing catalysts.

CRediT authorship contribution statement

Hyuk Choi: Writing – original draft, Visualization, Validation, Software, Investigation, Formal analysis, Data curation. **Yejung Choi:** Visualization, Investigation, Formal analysis, Data curation. **Jongseok**

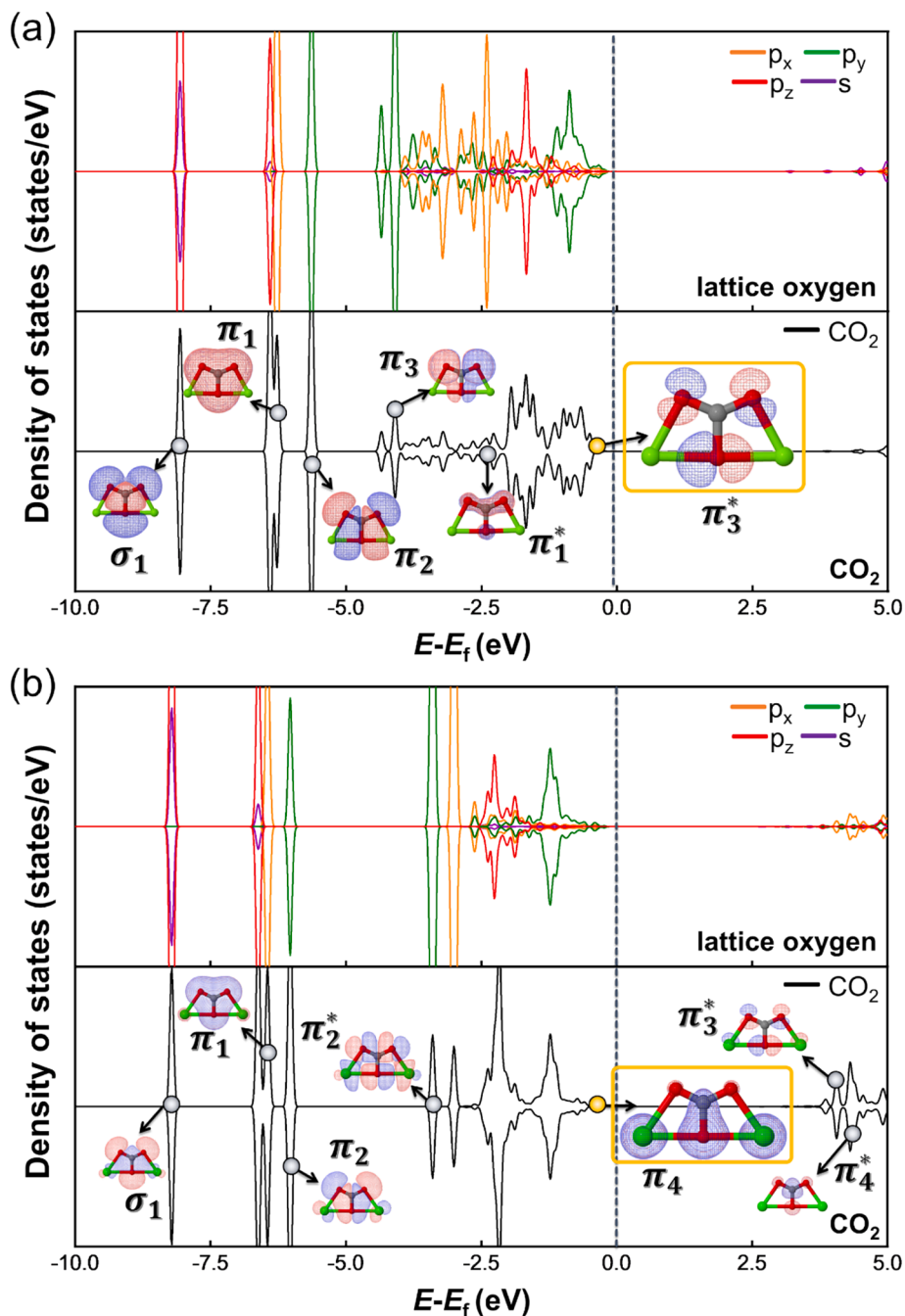


Fig. 7. Projected DOS plots of oxygen (above, colored) and CO_2 (below, black). Corresponding frontier orbitals of adsorbed CO_2 are accordingly presented. (a) MgO and (b) CaO. The yellow circles indicate the HOMOs of adsorbed CO_2 on oxide supports.

Kim: Visualization, Investigation, Formal analysis, Data curation. **Ju Hyeok Lee:** Visualization, Investigation, Formal analysis, Data curation. **Eunji Kang:** Validation, Investigation, Data curation. **Jieun Yun:** Data curation. **Hongjin Park:** Data curation. **Minkyung Kim:** Data curation. **Habib Ullah:** Data curation. **Kihyun Shin:** Writing – review & editing, Validation, Supervision. **Hyun You Kim:** Writing – review & editing, Supervision, Resources, Project administration, Funding acquisition, Conceptualization.

Declaration of competing interest

The authors declare that they have no known competing financial interests or personal relationships that could have appeared to influence the work reported in this paper.

Acknowledgments

H.Y.K acknowledges the financial support by the National Research Foundation of Korea (NRF) grant funded by the Korean government (Ministry of Science and ICT, MSIT, Korea) (2023R1A2C2008117), the Basic Science Research Program through the NRF funded by the Ministry of Education (RS-2021-NR060128), and the National R&D Program through the NRF funded by MSIT (2021M3H4A3A01050378). This work was supported by the BK21 Four Program by Chungnam National University Research Grant, 2022. Computing time was provided by the National Institute of Supercomputing and Network/Korea Institute of Science and Technology Information (KSC-2024-CRE-0118).

Appendix A. Supplementary data

Supplementary data to this article can be found online at <https://doi.org/10.1016/j.cej.2024.158163>.

Data availability

Data will be made available on request.

References

- [1] From Paris to Glasgow, *Nat. Catal.* 4 (11) (2021) 913–914.
- [2] Research in support of COP26. Naturehttps://www.nature.com/collections/hfggdbdee (11 October 2021).
- [3] J. Tollefson, *Nature* (2021) 589.
- [4] Global climate strike, *Nat. Catal.* 2 (10) (2019) 831.
- [5] C. Vogt, M. Monai, G.J. Kramer, B.M. Weckhuysen, The renaissance of the Sabatier reaction and its applications on Earth and in space, *Nat. Catal.* 2 (3) (2019) 188–197.
- [6] H. Yang, C. Zhang, P. Gao, H. Wang, X. Li, L. Zhong, W. Wei, Y. Sun, A review of the catalytic hydrogenation of carbon dioxide into value-added hydrocarbons, *Catal. Sci. Techno.* 7 (20) (2017) 4580–4598.
- [7] J. Qiao, Y. Liu, F. Hong, J. Zhang, A review of catalysts for the electroreduction of carbon dioxide to produce low-carbon fuels, *Chem. Soc. Rev.* 43 (2) (2014) 631–675.
- [8] Gao, J.; Choo Sze Shiong, S.; Liu, Y., Reduction of CO₂ to chemicals and Fuels: Thermocatalysis versus electrocatalysis. *Chem. Eng. J.* 2023, 472, 145033.
- [9] M. Wang, P. Wang, G. Zhang, Z. Cheng, M. Zhang, Y. Liu, R. Li, J. Zhu, J. Wang, K. Bian, Y. Liu, F. Ding, T.P. Senftle, X. Nie, Q. Fu, C. Song, X. Guo, Stabilizing Co₂C with H₂O and K promoter for CO₂ hydrogenation to C₂₊ hydrocarbons, *Sci. Adv.* 9 (24) (2023).
- [10] W. Zhou, K. Cheng, J. Kang, C. Zhou, V. Subramanian, Q. Zhang, Y. Wang, New horizon in C1 chemistry: breaking the selectivity limitation in transformation of syngas and hydrogenation of CO₂ into hydrocarbon chemicals and fuels, *Chem. Soc. Rev.* 48 (12) (2019) 3193–3228.
- [11] S. Roy, A. Cherevotan, S.C. Peter, Thermochemical CO₂ Hydrogenation to Single Carbon Products: Scientific and Technological Challenges, *ACS. Energy. Lett.* 3 (8) (2018) 1938–1966.
- [12] R.G. Rao, R. Blume, M.T. Greiner, P. Liu, T.W. Hansen, K.S. Dreyer, D.D. Hibbitts, J.-P. Tessonnier, Oxygen-Doped Carbon Supports Modulate the Hydrogenation Activity of Palladium Nanoparticles through Electronic Metal-Support Interactions, *ACS. Catal.* 12 (12) (2022) 7344–7356.
- [13] F. Liao, Y. Huang, J. Ge, W. Zheng, K. Tedsree, P. Collier, X. Hong, S.C. Tsang, Morphology-Dependent Interactions of ZnO with Cu Nanoparticles at the Materials' Interface in Selective Hydrogenation of CO₂ to CH₃OH, *Angew. Chem. Int. Ed.* 50 (9) (2011) 2162–2165.
- [14] S.R. Docherty, C. Copéret, Deciphering Metal–Oxide and Metal–Metal Interplay via Surface Organometallic Chemistry: A Case Study with CO₂ Hydrogenation to Methanol, *J. Am. Chem. Soc.* 143 (18) (2021) 6767–6780.
- [15] L.-X. Wang, L. Wang, F.-S. Xiao, Tuning product selectivity in CO₂ hydrogenation over metal-based catalysts, *Chem. Sci.* 12 (44) (2021) 14660–14673.
- [16] Q. Liu, X. Yang, L. Li, S. Miao, Y. Li, Y. Li, X. Wang, Y. Huang, T. Zhang, Direct catalytic hydrogenation of CO₂ to formate over a Schiff-base-mediated gold nanocatalyst, *Nat. Commun.* 8 (1) (2017) 1407.
- [17] J. Kim, H. Ha, W.H. Doh, K. Ueda, K. Mase, H. Kondoh, B.S. Mun, H.Y. Kim, J. Y. Park, How Rh surface breaks CO₂ molecules under ambient pressure, *Nat. Commun.* 11 (1) (2020) 5649.
- [18] Y. Guo, S. Mei, K. Yuan, D.-J. Wang, H.-C. Liu, C.-H. Yan, Y.-W. Zhang, Low-Temperature CO₂ Methanation over CeO₂-Supported Ru Single Atoms, Nanoclusters, and Nanoparticles Competitively Tuned by Strong Metal-Support Interactions and H-Spillover Effect, *ACS. Catal.* 8 (7) (2018) 6203–6215.
- [19] J. Zhou, Z. Gao, G. Xiang, T. Zhai, Z. Liu, W. Zhao, X. Liang, L. Wang, Interfacial compatibility critically controls Ru/TiO₂ metal-support interaction modes in CO₂ hydrogenation, *Nat. Commun.* 13 (1) (2022) 327.
- [20] Y. Wang, L.R. Winter, J.G. Chen, B. Yan, CO₂ hydrogenation over heterogeneous catalysts at atmospheric pressure: from electronic properties to product selectivity, *Green. Chem.* 23 (1) (2021) 249–267.
- [21] H. Zhao, R. Yu, S. Ma, K. Xu, Y. Chen, K. Jiang, Y. Fang, C. Zhu, X. Liu, Y. Tang, L. Wu, Y. Wu, Q. Jiang, P. He, Z. Liu, L. Tan, The role of Cu_{1–}O₃ species in single-atom Cu/ZrO₂ catalyst for CO₂ hydrogenation, *Nat. Catal.* 5 (9) (2022) 818–831.
- [22] M.S. Frei, C. Mondelli, R. García-Muelas, J. Morales-Vidal, M. Philipp, O. V. Safonova, N. López, J.A. Stewart, D.C. Ferré, J. Pérez-Ramírez, Nanostructure of nickel-promoted indium oxide catalysts drives selectivity in CO₂ hydrogenation, *Nat. Commun.* 12 (1) (2021) 1960.
- [23] C. Shen, K. Sun, Z. Zhang, N. Rui, X. Jia, D. Mei, C.-J. Liu, Highly Active Ir/In₂O₃ Catalysts for Selective Hydrogenation of CO₂ to Methanol: Experimental and Theoretical Studies, *ACS. Catal.* 11 (7) (2021) 4036–4046.
- [24] J. Wang, G. Zhang, J. Zhu, X. Zhang, F. Ding, A. Zhang, X. Guo, C. Song, CO₂ Hydrogenation to Methanol over In₂O₃-Based Catalysts: From Mechanism to Catalyst Development, *ACS. Catal.* 11 (3) (2021) 1406–1423.
- [25] M.A. Nolen, S.A. Tacey, S. Kwon, C.A. Farberow, Theoretical assessments of CO₂ activation and hydrogenation pathways on transition-metal surfaces, *Appl. Surf. Sci.* 637 (2023) 157873.
- [26] D. Cornu, H. Guesmi, J.-M. Krafft, H. Lauron-Pernot, Lewis Acidic-Basic Interactions between CO₂ and MgO Surface: DFT and DRIFT Approaches, *J. Phys. Chem. c.* 116 (11) (2012) 6645–6654.
- [27] W. Liao, C. Tang, H. Zheng, J. Ding, K. Zhang, H. Wang, J. Lu, W. Huang, Z. Zhang, Tuning activity and selectivity of CO₂ hydrogenation via metal-oxide interfaces over ZnO-supported metal catalysts, *J. Catal.* 407 (2022) 126–140.
- [28] Z. Zhang, L. Zhang, S. Yao, X. Song, W. Huang, M.J. Hulsey, N. Yan, Support-dependent rate-determining step of CO₂ hydrogenation to formic acid on metal oxide supported Pd catalysts, *J. Catal.* 376 (2019) 57–67.
- [29] M.B. Jensen, L.G.M. Pettersson, O. Swang, U. Olsbye, CO₂ Sorption on MgO and CaO Surfaces: A Comparative Quantum Chemical Cluster Study, *J. phys. Chem. b.* 109 (35) (2005) 16774–16781.
- [30] J. Przepiórski, A. Czyżewski, R. Pietrzak, B. Tryba, MgO/CaO-loaded porous carbons for carbon dioxide capture, *J. Therm. Anal. calorim.* 111 (1) (2013) 357–364.
- [31] J. Ilsemann, M.M. Murshed, T.M. Gesing, J. Kopyscinski, M. Bäumer, On the support dependency of the CO₂ methanation – decoupling size and support effects, *Catal. Sci. Technol.* 11 (12) (2021) 4098–4114.
- [32] Di Cosimo, J. I.; Diez, V. K.; Xu, M.; Iglesia, E.; Apesteguía, C. R., Structure and Surface and Catalytic Properties of Mg-Al Basic Oxides. *J.Catal.* 1998, 178 (2), 499–510.
- [33] S. Kawi, Y. Kathiraser, CO₂ as an Oxidant for High-Temperature Reactions, *Front. Energy Res.* 3 (2015).
- [34] C.-H. Shin, H.-Y. Lee, C. Gyan-Barimah, J.-H. Yu, J.-S. Yu, Magnesium: properties and rich chemistry for new material synthesis and energy applications, *Chem. Soc. Rev.* 52 (6) (2023) 2145–2192.
- [35] A. Cao, Z. Wang, H. Li, A.O. Elnabawy, J.K. Nørskov, New insights on CO and CO₂ hydrogenation for methanol synthesis: The key role of adsorbate-adsorbate interactions on Cu and the highly active MgO-Cu interface, *J. Catal.* 400 (2021) 325–331.
- [36] T. Haga, J.-I. Ozaki, K. Suzuki, Y. Nishiyama, Role of MgO and CaO promoters in Ni-catalyzed hydrogenation reactions of CO and carbon, *J. Catal.* 134 (1) (1992) 107–117.
- [37] G. Wang, Y. Guo, J. Yu, F. Liu, J. Sun, X. Wang, T. Wang, C. Zhao, Ni-CaO dual function materials prepared by different synthetic modes for integrated CO₂ capture and conversion, *Chem. Eng. J.* 428 (2022) 132110.
- [38] J. Hu, P. Hongmanorom, P. Chirawatkul, S. Kawi, Efficient integration of CO₂ capture and conversion over a Ni supported CeO₂-modified CaO microsphere at moderate temperature, *Chem. Eng. J.* 426 (2021) 130864.
- [39] H. Kang, L. Zhu, S. Li, S. Yu, Y. Niu, B. Zhang, W. Chu, X. Liu, S. Perathoner, G. Centi, Y. Liu, Generation of oxide surface patches promoting H-spillover in Ru/(TiO_x)MnO catalysts enables CO₂ reduction to CO, *Nat. Catal.* 6 (11) (2023) 1062–1072.
- [40] K. Murakami, Y. Sekine, Recent progress in use and observation of surface hydrogen migration over metal oxides, *Physical Chemistry Chemical Physics* 22 (40) (2020) 22852–22863.
- [41] D.R. Aireddy, K. Ding, Heterolytic Dissociation of H₂ in Heterogeneous Catalysis, *ACS. Catal.* 12 (8) (2022) 4707–4723.
- [42] W. Karim, C. Spreafico, A. Kleibert, J. Gobrecht, J. VandeVondele, Y. Ekinci, J. A. van Bokhoven, Catalyst support effects on hydrogen spillover, *Nature* 541 (7635) (2017) 68–71.
- [43] K. Shun, K. Mori, S. Masuda, N. Hashimoto, Y. Hinuma, H. Kobayashi, H. Yamashita, Revealing hydrogen spillover pathways in reducible metal oxides, *Chem. Sci.* 13 (27) (2022) 8137–8147.
- [44] T. Whittaker, K.B.S. Kumar, C. Peterson, M.N. Pollock, L.C. Grabow, B. D. Chandler, H₂ Oxidation over Supported Au Nanoparticle Catalysts: Evidence for Heterolytic H₂ Activation at the Metal-Support Interface, *J. Am. Chem. Soc.* 140 (48) (2018) 16469–16487.
- [45] A.S. Crampton, M.D. Rötzer, C.J. Ridge, F.F. Schweinberger, U. Heiz, B. Yoon, U. Landman, Structure sensitivity in the nonscalable regime explored via catalysed ethylene hydrogenation on supported platinum nanoclusters, *Nat. Commun.* 7 (1) (2016) 10389.
- [46] Z. Yan, A. Tomer, G. Perrussel, M. Ousmane, B. Katryniok, F. Dumeignil, A. Ponchel, A. Liebens, M. Pera-Titus, A Pd/CeO₂ “H₂ Pump” for the Direct Amination of Alcohols, *Chem. Cat. Chem.* 8 (21) (2016) 3347–3352.
- [47] Y. An, P. Chatterjee, P. Naik, S. Banerjee, W. Huang, I.I. Slowing, V. Venditti, Hydrogen spillover and substrate-support hydrogen bonding mediate hydrogenation of phenol catalyzed by palladium on reducible metal oxides, *Chem. Sci.* 14 (48) (2023) 14166–14175.
- [48] G. Perego, Characterization of heterogeneous catalysts by X-ray diffraction techniques, *Catal. Today.* 41 (1–3) (1998) 251–259.
- [49] K. Liu, A. Wang, T. Zhang, Recent Advances in Preferential Oxidation of CO Reaction over Platinum Group Metal Catalysts, *ACS. Catal.* 2 (6) (2012) 1165–1178.
- [50] X.J. Cui, W. Li, P. Ryabchuk, K. Junge, M. Beller, Bridging homogeneous and heterogeneous catalysis by heterogeneous single-metal-site catalysts, *Nat. Catal.* 1 (6) (2018) 385–397.
- [51] H. Ha, S. Yoon, K. An, H.Y. Kim, Catalytic CO oxidation over Au nanoparticles supported on CeO₂ nanocrystals: Effect of the Au-CeO₂ interface, *ACS. Catal.* 8 (2018) 11491–11501.
- [52] M. Kottwitz, Y.Y. Li, H.D. Wang, A.I. Frenkel, R.G. Nuzzo, Single Atom Catalysts: A Review of Characterization Methods, *Chem. Methods.* 1 (6) (2021) 278–294.
- [53] Q. Zhang, S.Q. Gao, J.H. Yu, Metal Sites in Zeolites: Synthesis, Characterization, and Catalysis, *Chem. Rev.* 123 (9) (2023) 6039–6106.
- [54] A. Parastaev, V. Muravev, E. Huertas Osta, A.J.F. van Hoof, T.F. Kimpel, N. Kosinov, E.J.M. Hensen, Boosting CO₂ hydrogenation via size-dependent

- metal–support interactions in cobalt/ceria-based catalysts, *Nat. Catal.* 3 (6) (2020) 526–533.
- [55] C. Hernández Mejía, T.W. van Deelen, K.P. de Jong, Activity enhancement of cobalt catalysts by tuning metal–support interactions, *Nat. Commun.* 9 (1) (2018) 4459.
- [56] Y. Lykhach, S.M. Kozlov, T. Skála, A. Tovt, V. Stetsovych, N. Tsud, F. Dvořák, V. Johánek, A. Neitzel, J. Mysliveček, S. Fabris, V. Matolín, K.M. Neyman, J. Libuda, Counting electrons on supported nanoparticles, *Nat. Mater.* 15 (3) (2016) 284–288.
- [57] A. Beck, X. Huang, L. Artiglia, M. Zabilskiy, X. Wang, P. Rzepka, D. Palagin, M.-G. Willinger, J.A. van Bokhoven, The dynamics of overlayer formation on catalyst nanoparticles and strong metal–support interaction, *Nat. Commun.* 11 (1) (2020) 3220.
- [58] G. Kresse, J. Furthmüller, Efficient iterative schemes for ab initio total-energy calculations using a plane-wave basis set, *Phys. Rev. b* 54 (16) (1996) 11169–11186.
- [59] J.P. Perdew, K. Burke, M. Ernzerhof, Generalized Gradient Approximation Made Simple, *Phys. Rev. Lett.* 77 (18) (1996) 3865–3868.
- [60] J. Klimes, A. Michaelides, Perspective: Advances and challenges in treating van der Waals dispersion forces in density functional theory, *J. Chem. Phys.* 137 (12) (2012) 120901.
- [61] P.E. Blochl, Projector Augmented-Wave Method, *Phys. Rev. b* 50 (24) (1994) 17953–17979.
- [62] G. Kresse, D. Joubert, From ultrasoft pseudopotentials to the projector augmented-wave method, *Phys. Rev. b* 59 (3) (1999) 1758–1775.
- [63] G. Henkelman, B.P. Uberuaga, H. Jónsson, A climbing image nudged elastic band method for finding saddle points and minimum energy paths, *J. Chem. Phys.* 113 (22) (2000) 9901–9904.
- [64] G. Henkelman, H. Jónsson, Improved tangent estimate in the nudged elastic band method for finding minimum energy paths and saddle points, *J. Chem. Phys.* 113 (22) (2000) 9978–9985.
- [65] S. Maintz, V.L. Deringer, A.L. Tchougreeff, R. Dronkowski, LOBSTER: A tool to extract chemical bonding from plane-wave based DFT, *J. Comput. Chem.* 37 (11) (2016) 1030–1035.
- [66] R. Nelson, C. Ertural, J. George, V.L. Deringer, G. Hautier, R. Dronkowski, LOBSTER: Local orbital projections, atomic charges, and chemical-bonding analysis from projector-augmented-wave-based density-functional theory, *J. Comput. Chem.* 41 (21) (2020) 1931–1940.
- [67] P.J. Linstrom, W.G. Mallard, The NIST Chemistry WebBook: A Chemical Data Resource on the Internet, *J. Chem. Eng. d* 46 (5) (2001) 1059–1063.
- [68] C.T. Campbell, J.R.V. Sellers, Enthalpies and Entropies of Adsorption on Well-Defined Oxide Surfaces: Experimental Measurements, *Chem. Rev.* 113 (6) (2013) 4106–4135.
- [69] S.K. Sharma, T.S. Khan, R.K. Singha, B. Paul, M.K. Poddar, T. Sasaki, A. Bordoloi, C. Samanta, S. Gupta, R. Bal, Design of highly stable MgO promoted Cu/ZnO catalyst for clean methanol production through selective hydrogenation of CO₂, *Appl. Catal. a: Gen.* 623 (2021) 118239.
- [70] S. Kattel, P. Liu, J.G. Chen, Tuning Selectivity of CO₂ Hydrogenation Reactions at the Metal/Oxide Interface, *J. Am. Chem. Soc.* 139 (29) (2017) 9739–9754.
- [71] R.W. Dorner, D.R. Hardy, F.W. Williams, B.H. Davis, H.D. Willauer, Influence of Gas Feed Composition and Pressure on the Catalytic Conversion of CO₂ to Hydrocarbons Using a Traditional Cobalt-Based Fischer–Tropsch Catalyst, *Energy & Fuels* 23 (8) (2009) 4190–4195.
- [72] X. Wang, H. Shi, J.H. Kwak, J. Szanyi, Mechanism of CO₂ Hydrogenation on Pd/Al₂O₃ Catalysts: Kinetics and Transient DRIFTS-MS Studies, *ACS. Catal.* 5 (11) (2015) 6337–6349.
- [73] X. Wang, C. Zeng, N. Gong, T. Zhang, Y. Wu, J. Zhang, F. Song, G. Yang, Y. Tan, Effective Suppression of CO Selectivity for CO₂ Hydrogenation to High-Quality Gasoline, *ACS. Catal.* 11 (3) (2021) 1528–1547.
- [74] Y. He, S. Liu, W. Fu, C. Wang, C. Mebrahtu, R. Sun, F. Zeng, Thermodynamic Analysis of CO₂ Hydrogenation to Higher Alcohols (C₂–OH): Effects of Isomers and Methane, *ACS Omega* 7 (19) (2022) 16502–16514.
- [75] K. Shin, L. Zhang, H. An, H. Ha, M. Yoo, H.M. Lee, G. Henkelman, H.Y. Kim, Interface engineering for a rational design of poison-free bimetallic CO oxidation catalysts, *Nanoscale* 9 (16) (2017) 5244–5253.
- [76] S. Li, Y. Xu, Y. Chen, W. Li, L. Lin, M. Li, Y. Deng, X. Wang, B. Ge, C. Yang, S. Yao, J. Xie, Y. Li, X. Liu, D. Ma, Tuning the Selectivity of Catalytic Carbon Dioxide Hydrogenation over Iridium/Cerium Oxide Catalysts with a Strong Metal–Support Interaction, *Angew. Chem. Int. Ed.* 129 (36) (2017) 10901–10905.
- [77] F. Arena, G. Italiano, K. Barbera, S. Bordiga, G. Bonura, L. Spadaro, F. Frusteri, Solid-state interactions, adsorption sites and functionality of Cu-ZnO/ZrO₂ catalysts in the CO₂ hydrogenation to CH₃OH, *Appl. Catal. a: Gen.* 350 (1) (2008) 16–23.
- [78] R. Satthawong, N. Koizumi, C. Song, P. Prasassarakich, Light olefin synthesis from CO₂ hydrogenation over K-promoted Fe–Co bimetallic catalysts, *Catal. Today* 251 (2015) 34–40.
- [79] Z. Zhang, Y. Liu, L. Jia, C. Sun, B. Chen, R. Liu, Y. Tan, W. Tu, Effects of the reducing gas atmosphere on performance of FeCeNa catalyst for the hydrogenation of CO₂ to olefins, *Chem. Eng. J.* 428 (2022) 131388.
- [80] M. Guo, G. Lu, The difference of roles of alkaline-earth metal oxides on silica-supported nickel catalysts for CO₂ methanation, *RSC. Adv.* 4 (102) (2014) 58171–58177.
- [81] C. Wang, Y. Fang, G. Liang, X. Lv, H. Duan, Y. Li, D. Chen, M. Long, Mechanistic study of Cu–Ni bimetallic catalysts supported by graphene derivatives for hydrogenation of CO₂ to methanol, *J. CO₂ Util.* 49 (2021) 101542.
- [82] X. Fang, Y. Men, F. Wu, Q. Zhao, R. Singh, P. Xiao, T. Du, P.A. Webley, Promoting CO₂ hydrogenation to methanol by incorporating adsorbents into catalysts: Effects of hydrotalcite, *Chem. Eng. J.* 378 (2019) 122052.
- [83] J. Xiao, D. Mao, X. Guo, J. Yu, Effect of TiO₂, ZrO₂, and TiO₂–ZrO₂ on the performance of CuO–ZnO catalyst for CO₂ hydrogenation to methanol, *Appl. Surf. Sci.* 338 (2015) 146–153.
- [84] C. Wu, L. Lin, J. Liu, J. Zhang, F. Zhang, T. Zhou, N. Rui, S. Yao, Y. Deng, F. Yang, W. Xu, J. Luo, Y. Zhao, B. Yan, X.-D. Wen, J.A. Rodriguez, D. Ma, Inverse ZrO₂/Cu as a highly efficient methanol synthesis catalyst from CO₂ hydrogenation, *Nat. Commun.* 11 (1) (2020) 5767.
- [85] X. Fang, Y. Men, F. Wu, Q. Zhao, R. Singh, P. Xiao, T. Du, P.A. Webley, Moderate-pressure conversion of H₂ and CO₂ to methanol via adsorption enhanced hydrogenation, *Int. J. Hydrogen. Energy.* 44 (39) (2019) 21913–21925.
- [86] M.S. Frei, M. Capdevila-Cortada, R. García-Muelas, C. Mondelli, N. López, J. A. Stewart, D. Curulla Ferré, J. Pérez-Ramírez, Mechanism and microkinetics of methanol synthesis via CO₂ hydrogenation on indium oxide, *J. catal.* 361 (2018) 313–321.
- [87] N. Koizumi, X. Jiang, J. Kugai, C. Song, Effects of mesoporous silica supports and alkaline promoters on activity of Pd catalysts in CO₂ hydrogenation for methanol synthesis, *Catal. Today* 194 (1) (2012) 16–24.
- [88] Y. Choi, S.K. Cha, H. Ha, S. Lee, H.K. Seo, J.Y. Lee, H.Y. Kim, S.O. Kim, W. Jung, Unravelling inherent electrocatalysis of mixed-conducting oxide activated by metal nanoparticle for fuel cell electrodes, *Nat. Nanotechnol.* 14 (3) (2019) 245–251.
- [89] H. Rong, S. Ji, J. Zhang, D. Wang, Y. Li, Synthetic strategies of supported atomic clusters for heterogeneous catalysis, *Nat. Commun.* 11 (1) (2020) 5884.
- [90] H. Zhang, X. Wang, P. Liu, Reaction-driven selective CO₂ hydrogenation to formic acid on Pd(111), *Phys. Chem. Chem. Phys.* 24 (28) (2022) 16997–17003.
- [91] Y. Wang, S. Kattel, W. Gao, K. Li, P. Liu, J.G. Chen, H. Wang, Exploring the ternary interactions in Cu–ZnO–ZrO₂ catalysts for efficient CO₂ hydrogenation to methanol, *Nat. Commun.* 10 (1) (2019) 1166.
- [92] W. Li, H. Wang, X. Jiang, J. Zhu, Z. Liu, X. Guo, C. Song, A short review of recent advances in CO₂ hydrogenation to hydrocarbons over heterogeneous catalysts, *RSC. Adv.* 8 (14) (2018) 7651–7669.
- [93] B. Hammer, Y. Morikawa, J.K. Nørskov, CO Chemisorption at Metal Surfaces and Overlays, *Phys. Rev. Lett.* 76 (12) (1996) 2141–2144.
- [94] B.H. Morrow, D.E. Resasco, A. Striolo, M.B. Nardelli, CO Adsorption on Noble Metal Clusters: Local Environment Effects, *J. Phys. Chem. c.* 115 (13) (2011) 5637–5647.
- [95] X. Ma, H. Xin, Orbitalwise Coordination Number for Predicting Adsorption Properties of Metal Nanocatalysts, *Phys. Rev. Lett.* 118 (3) (2017) 036101.
- [96] G. Marek, E. Andreas, H. Jürgen, CO adsorption on close-packed transition and noble metal surfaces: trends from ab initio calculations, *J. Phys. Condens. Matter.* 16 (8) (2004) 1141.
- [97] R. Ismail, M.A.H. Saad, M.J. Al-Marri, A. Sardar, A.T. Mohamed, M. El-Naas, A.M. S. Soliman, A. Benamor, Synthesis and evaluation of novel Cu-based adsorbent-containing catalysts for CO₂ hydrogenation to methanol and value-added products, *J. Environ. Chem. Eng.* 12 (2) (2024) 112325.
- [98] S.K. Sharma, B. Paul, A. Srivastava, R.S. Pal, M.K. Poddar, T.S. Khan, C. Samanta, R. Bal, The role of MgO during CO₂ hydrogenation to methanol over Pd/ZnO catalyst, *S. Chem. for Climate Action* 2 (2023) 100019.
- [99] Y. Song, X. Liu, L. Xiao, W. Wu, J. Zhang, X. Song, Pd-Promoter/MCM-41: A Highly Effective Bifunctional Catalyst for Conversion of Carbon Dioxide, *Catal. Lett.* 145 (6) (2015) 1272–1280.
- [100] J.C. Davies, R. Nielsen, L.B. Thomsen, I. Chorkendorff, A. Logadottir, Z. Lodzianna, J.K. Nørskov, W. Li, B. Hammer, S.J.F.C. Longwitz, CO desorption rate dependence on CO partial pressure over platinum fuel cell catalysts, *Fuel. Cells.* 4 (4) (2004) 309–319.